STRUCTURAL BIOLOGY

The pore conformation of lymphocyte perforin

Marina E. Ivanova[1,2], Natalya Lukoyanova[1], Sony Malhotra[1,3], Maya Topf[1,4], Joseph A. Trapani[5], Ilia Voskoboinik[5], Helen R. Saibil[1]*

Perforin is a pore-forming protein that facilitates rapid killing of pathogen-infected or cancerous cells by the immune system. Perforin is released from cytotoxic lymphocytes, together with proapoptotic granzymes, to bind to a target cell membrane where it oligomerizes and forms pores. The pores allow granzyme entry, which rapidly triggers the apoptotic death of the target cell. Here, we present a 4-Å resolution cryo–electron microscopy structure of the perforin pore, revealing previously unidentified inter- and intramolecular interactions stabilizing the assembly. During pore formation, the helix-turn-helix motif moves away from the bend in the central β sheet to form an intermolecular contact. Cryo–electron tomography shows that prepores form on the membrane surface with minimal conformational changes. Our findings suggest the sequence of conformational changes underlying oligomerization and membrane insertion, and explain how several pathogenic mutations affect function.

INTRODUCTION

Cytotoxic T lymphocytes (CTLs) and natural killer (NK) cells are essential for survival because they eliminate viral infection or destroy cancerous cells (*1*, *2*). To kill target cells, activated CTLs synthesize secretory vesicles (colloquially known as "lytic granules") containing the pore-forming protein perforin (*3*–*5*) and proapoptotic serine proteases granzymes (*6*). CTLs form tight contacts, known as immune synapses, with virally infected or transformed cells, and release the contents of lytic granules by exocytosis into the immune synapse (*7*). In the extracellular medium, which contains 1 to 1.3 mM free Ca^{2+}, perforin binds to the target cell plasma membrane where it oligomerizes into arcs and rings, and transforms into pores that allow the entry of granzymes, triggering apoptosis (*8*–*10*). An alternate pathway has been proposed in which perforin is internalized by endocytosis and then forms pores from inside endocytic vesicles to release the granzymes (*11*). In either case, perforin must bind to a membrane to form oligomeric pores.

Complete congenital loss of perforin function invariably results in type 2 familial hemophagocytic lymphohistiocytosis (FHL)—a life-threatening autosomal recessive disorder that ultimately stems from cytokine hypersecretion and uncontrolled macrophage activation (*12*); if left untreated, the median survival of individuals who inherit two null perforin alleles is just 2 months (*13*). Hypomorphic perforin mutations are associated with atypical/late-onset FHL (*14*), lymphoma, and other cancers (*15*–*18*).

Perforin is a member of the membrane attack complex perforin/cholesterol-dependent cytolysin (MACPF/CDC) superfamily of pore-forming proteins (*19*–*21*). Members of this superfamily are found in all kingdoms of life and are involved in diverse processes including toxic attack (*22*), immune defense (*23*), development (*24*), pathogen invasion (*25*), and inflammation (*26*). These proteins characteristically undergo a major conformational change to convert water-soluble monomers into oligomeric transmembrane pores. The conserved MACPF domain consists of a central, bent β sheet and three helical regions: two α-helical bundles known as transmembrane hairpins (TMHs) 1 and 2, and a third helical bundle termed helix-turn-helix (HTH) motif. Although the core MACPF domain topology is conserved, the surrounding domains are highly divergent. Upon membrane docking, TMH1 and TMH2 extend into amphipathic β hairpins that assemble into a giant β barrel spanning the target cell membrane (*27*). It is still unclear what signal triggers the transition between soluble and pore conformations, but it has been shown that before membrane insertion many MACPF/CDC proteins oligomerize into circular prepores—a pore precursor assembly that binds the membrane but is not inserted (*28*). It is not always necessary to assemble a complete ring, as arcs and incomplete rings have been shown to perforate the membranes in vitro (*29*–*31*). Other members of the MACPF/CDC family such as the membrane attack complex (MAC) do not form a prepore and are able to add subunits after the initial complex has been inserted (*32*, *33*).

The structure of the soluble form of perforin was previously solved by x-ray crystallography (*34*). The perforin subunit consists of three domains: the conserved MACPF domain, the membrane-docking C2 domain, and the epidermal growth factor (EGF)–like domain (Fig. 1A). Structures of several MACPF and MACPF-like proteins in the membrane-bound state, such as the MAC (*32*), the macrophage protein perforin-2/MPEG-1 (*35*, *36*), and the more distantly related gasdermin A3 (*37*), have been determined by cryo–electron microscopy (cryo-EM) with near-atomic resolution, but they are quite divergent in structure and do not host the sites of pathogenic mutations found in perforin. Here, we present the structure of the perforin pore, revealing its unique domain movements and explaining why some of the clinically relevant mutations are deleterious for function, including some centrally involved in the conformational transition.

RESULTS

Molecular architecture of a perforin pore

Murine wild-type (WT) perforin was recombinantly expressed and purified from baculovirus-infected insect cells as described previously (*38*). Perforin pores were assembled on phosphatidylcholine (PC) liposomes, in the presence of $CaCl_2$ (see Methods). Detergent screening

[1]Institute of Structural and Molecular Biology, Birkbeck, University of London, Malet St, London WC1E 7HX, UK. [2]Imperial College London, Hammersmith Campus, Du Cane Road, London W12 0NN, UK. [3]Scientific Computing Department, Science and Technology Facilities Council, Rutherford Appleton Laboratory, Fermi Ave, Harwell, Didcot OX11 0QX, UK. [4]Centre for Structural Systems Biology, Leibniz-Institut für Experimentelle Virologie and Universitätsklinikum Hamburg-Eppendorf (UKE), Hamburg, Germany. [5]Peter MacCallum Cancer Centre, 305 Grattan St, Melbourne, VIC 3000, Australia.
*Corresponding author. Email: h.saibil@bbk.ac.uk

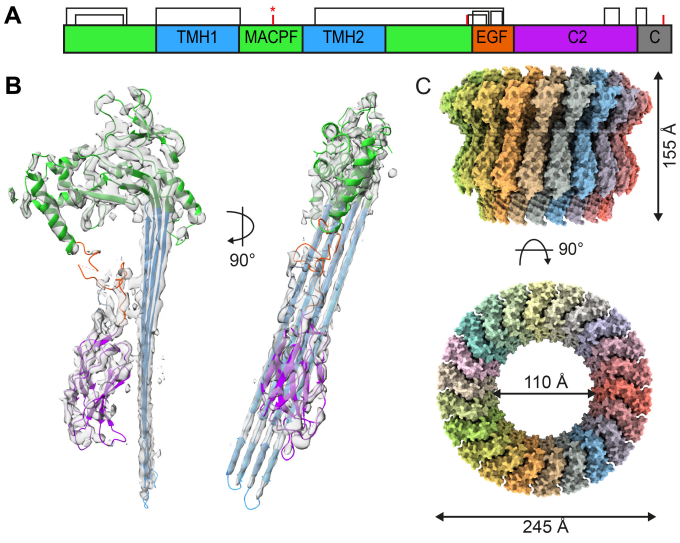

Fig. 1. Overview of perforin structure. (**A**) Domain structure of perforin. Disulfide bonds are indicated by black brackets, glycosylation sites by red bars, and N204 glycosylation site by a red asterisk. (**B**) Fitting of the perforin model into the density corresponding to an inserted subunit. (**C**) Overview of the perforin pore with C22 symmetry.

identified the commonly used detergent Triton X-100 as the best solubilizing agent for perforin pores, as shown by negative-stain EM (fig. S1A). The detergent solubilized samples mainly contained complete perforin rings, suggesting that the incomplete rings, usually abundant in perforin pore preparations (*10*), are unstable in the presence of Triton X-100.

We used single-particle cryo-EM to determine the structure of the solubilized perforin pore. Inspection of two-dimensionally (2D) classified top views of perforin pores revealed particles with symmetry ranging from C15 to C26, with most having 21- to 23-fold symmetry (fig. S2). Because of flexibility and size heterogeneity of the pores, particle subtraction followed by focused refinement was implemented to extract and resolve a wedge of the perforin pore, with a final resolution of 4.0 Å. The local resolution of the map ranged from 3.9 to 6.7 Å, with the β barrel being the best-defined feature (fig. S1, D and E). This map was used to build a molecular model of the perforin pore (Fig. 1A).

The 22-fold perforin pore has a diameter of ~245 Å and height of ~155 Å (Fig. 1B). The narrowest part of the pore has an opening of ~110 Å in diameter, which is sufficient to allow passage of a granzyme B monomer or a granzyme A dimer into the target cell. The MACPF, EGF-like, and C2 domains of perforin are outside the pore, while the luminal side is composed of a giant β barrel with a diameter of ~145 Å and a height of ~125 Å. An earlier study based on low-resolution data and labeling of sites in the perforin C terminus suggested that the orientation of the perforin molecule in the pore is reversed relative to other members of the CDC/MACPF superfamily (*34*). Although that orientation has always seemed unlikely, no further experimental evidence on perforin has emerged to establish the orientation until now. The C-terminal tail of perforin is not ordered in our structure, and it has been previously shown that this region is very flexible and cleaved during maturation (*39*, *40*). The overall architecture of the perforin molecule is supported by nine disulfide bonds that are scattered over all domains (Fig. 1A). Three perforin glycosylation sites have been previously reported: N204, N375, and N548 (*41*), but density for only N204 glycosylation is observed in the pore structure.

Each perforin subunit contributes four antiparallel β strands toward assembly of the β barrel. The bottom 30 Å of the β barrel forms the transmembrane pore, with the rest of the perforin ring located above the lipid bilayer (Fig. 2A). The β strands enter the membrane at an angle of ~18° to the pore axis, making the right-handed twist characteristic of β barrels formed by L-amino acids. There is a two-residue shift in register between adjacent subunits (fig. S1E), giving a shear number of 44 for the 22-fold symmetric pore, which equals the total number of antiparallel β strands in the circular structure. This agrees well with theoretical predictions of giant β-barrel architecture (*42*, *43*). The membrane-facing portion of the β barrel is lined by mostly hydrophobic side chains, whereas the luminal side is mostly hydrophilic (fig. S1F).

The narrowest part of the pore is formed by the HTH motif, which is enriched in negatively charged residues (fig. S1G). It has been previously shown that perforin pores show a preference for cationic cargos over neutral or negatively charged ones (*44*). In comparison, the streptolysin O pore contains both positively and negatively charged amino acids in its HTH motif and is able to deliver a wide range of molecules irrespective of charge, although its wider diameter may lessen any charge effects (fig. S1G) (*45*). A recent study of the gasdermin D pore shows that a charged lining in a pore of similar diameter to perforin confers substrate selectivity (*46*). In the perforin HTH motif, D308, D312, and E322 form a negatively charged ring on the luminal side of the pore, which may facilitate diffusion of granzyme B into the target cell. Notably, D312 is conserved in higher vertebrates and a mutation of this residue to valine (D313V in human perforin) has been found in a cancer patient (*47*). Human and murine perforin share 68% identity; the human protein has one additional residue at the cleaved signaling N-terminal peptide. While expression levels of this mutant perforin are comparable to those of the WT perforin, the lytic activity is reduced sevenfold in the context of mouse perforin.

Conformational transition upon membrane insertion

Comparison of soluble and pore conformations reveals a major reorganization of the protein upon membrane insertion (Fig. 2). The upper part of the MACPF domain is quite rigid and remains largely unchanged; superposition of the soluble and inserted forms of the protein gave a root mean square deviation (RMSD) of 1.65 Å over 189 Cα atoms in this region (Fig. 2A). The main conformational change happens in the lower part of the MACPF domain, where helices comprising TMH1 and TMH2 regions refold to form antiparallel membrane-spanning β strands (Fig. 2B). At the same time, the central β sheet unbends by 17° (fig. S3A). The EGF-like domain, which acts as a linker between the MACPF domain and the membrane-associated C2 domain, is covalently bound to TMH2 through the disulfide bond between Cys^{407} and Cys^{241}. Upon membrane insertion, TMH2 pulls the EGF domain 10 Å toward the newly assembled β barrel (Fig. 2C) so that the EGF domain fills in the space previously occupied by TMH1. EGF-like domains are characterized by the presence of three or four canonical disulfide bonds (*48*), but the loops connecting conserved cysteines greatly vary in length and structure and can adopt a range of conformations, resulting in a very flexible architecture.

The helical arrangement of TMH1 and TMH2 in the soluble form of the protein is stabilized by an extensive network of hydrogen

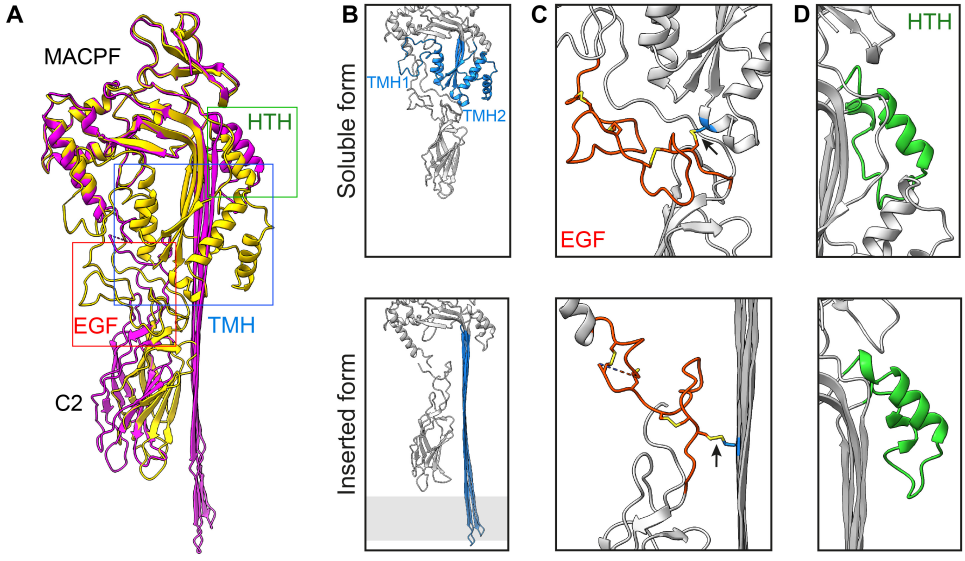

Fig. 2. Conformational change of perforin upon insertion into the membrane. (**A**) Superimposition of soluble [yellow, Protein Data Bank (PDB) code 3NSJ] and inserted (magenta) models of perforin. (**B** to **D**) Structural comparison of TMH regions (B), EGF domain (C), and HTH motif (D) in soluble (left) and inserted (right) forms of perforin. In (B), the membrane position is indicated in gray. For (B) to (D), domains are colored according to the labels in (A) (HTH, green; TMH, blue; EGF, red) and the rest of the structure (inserted or soluble) is in gray. In (C), the disulfide bond between the EGF and TMH is shown in yellow and indicated by arrows.

bonds formed between this part of the molecule and adjacent domains: the upper part of MACPF domain, EGF-like domain, and C-terminal tail (fig. S3B). With the extrusion of TMH1 and TMH2, the flexible EGF domain and C-terminal tail make few contacts and become extremely mobile so that they could not be accurately fitted in the density. Therefore, the structures of the EGF domain and C terminus are less reliable than other parts of the molecule. Of the residues making interactions with TMH1 and TMH2 in the soluble form of the protein, many are mutated in FHL patients (mutations R54C, H222R, H222Q, R361W, R410P, and R410W in human numbering) (*2*, *47*, *49*). Two of these residues (H222 and R361) are conserved from fish to humans (fig. S4). Expression of the H222R mutant was shown to be undetectable or greatly reduced compared to the WT protein, suggesting that this mutation leads to protein misfolding, whereas the mouse forms of H222Q and R361W variants were expressed in rat basophilic leukemia (RBL) cells at levels equivalent to WT perforin (*50*, *51*). RBL cells transfected with H222Q mutant mouse protein had no detectable cytotoxic activity (*50*), suggesting that this mutation affects the function of the protein rather than its stability. The structure of mouse perforin in its soluble form shows that the side chain of the equivalent residue (H221) makes a hydrogen bond with the main-chain oxygen of W128, which is located in the loop between the two helices in TMH1. Substitution of histidine by (similarly sized) glutamine does not perturb the overall architecture of the molecule but allows the formation of a stronger hydrogen bond with W128, which, in turn, disfavors the conformational transition required for membrane insertion of the mutant molecule. The loss of pore-forming activity confirms that H222 is important for perforin function in disrupting the target cell membrane.

Another notable conformational change happens on the luminal side of the pore. The second helix in the third helical bundle, which is unfolded in the soluble monomer, assembles to form three helical turns completing the HTH motif facing the lumen of the pore at the top of the β barrel (Fig. 2D). The HTH moves up slightly and tilts by 6° away from the bend of the central β sheet, a displacement that was previously proposed to unlock the conformational change needed for membrane insertion (*52*). This movement is supported by the movement of the side chain of R298, which makes a new interaction with the bottom loop of the HTH motif (fig. S3C). In the soluble form of perforin, R298 makes a hydrogen bond interaction with the main-chain oxygens of H292 and Y295 stabilizing the turn between the central β sheet and helices of TMH2. R298 is absolutely conserved from fish to humans (fig. S4). This residue has been found to be mutated in FHL patients, and this mutation has a detrimental effect on perforin expression and NK cell function (*47*, *50*).

Oligomerization interface

The primary oligomerization interface is located on the flat face of the globular MACPF domain of perforin. It has been previously shown that E343 of one subunit interacts with R213 on the adjacent monomer (*34*), and that a salt bridge linking the two residues is indispensable for lytic function (*53*). The structure of the inserted form of perforin shows that these two residues are located in close proximity to each other, with Arg and Glu side chains pointing toward each other (Fig. 3A). Reversing the charge of either one of these residues causes complete loss of function, but reversing both of them restores WT function (*53*). A number of other charged residues are located on the flat surface of the MACPF domain and are likely to contribute toward the overall intermolecular affinity.

The second oligomerization interface is formed by the HTH motif, mentioned above, on the luminal side of the pore. The HTH motif is formed by an insertion at the bend of the central β sheet, and it must be displaced away from the core of the MACPF domain for the TMH2 helices to refold into β hairpins. Once displaced, it adopts a new conformation that is supported by the hydrogen bond formed between the side chain of R103 from a β-hairpin of one subunit

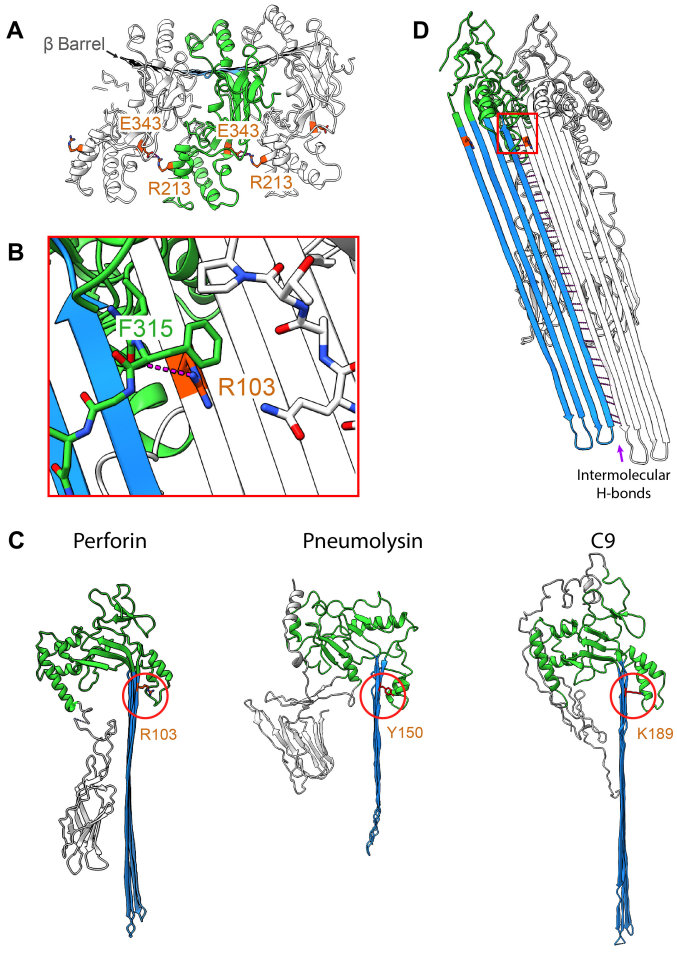

Fig. 3. Oligomerization interface. (**A**) Top view of the perforin oligomer; the central perforin subunit is highlighted in green, with residues making intermolecular interactions in orange. (**B**) Oligomerization interface in the β barrel, with one subunit shown in color and the adjacent one in gray. Intermolecular hydrogen bonds are shown in pink. (**C**) Secondary oligomerization interface formed between HTH motif of one subunit (shown in color) and Arg^{103} in the β barrel of the next (shown in light gray; Arg^{103} is highlighted in orange). This region is highlighted with a red box in (C). (**D**) Comparison of perforin with other MACPF proteins, with the residues equivalent to Arg^{103} of perforin (Tyr^{150} and Lys^{189} of pneumolysin and C9, respectively) circled in red and shown in red sticks.

and the main-chain oxygen of F315 located at the HTH turn of the adjacent subunit (Fig. 3B). Comparison with other members of the MACPF family showed that this interaction is conserved between different pore-forming proteins with a tyrosine or a lysine located at equivalent positions at the top of the first β-hairpin (Fig. 3C).

Last, once TMH1 and TMH2 transition from α helices to β strands, the third, and strongest, oligomerization interface is formed by β hairpins from adjacent monomers. Antiparallel β strands form the β barrel via an extensive network of hydrogen bonds between the main-chain atoms of neighboring strands (Fig. 3D). Giant β barrels can adopt variable curvature, allowing the pores to be built with a wide range of symmetries and pore diameters. The height of the hydrophobic belt is ~30 Å, consistent with the barrel completely traversing the hydrophobic region of a lipid bilayer.

Cryo–electron tomography of perforin prepores

We previously showed that before membrane insertion perforin molecules can form prepores—oligomers docked on but not inserted into membranes, typically consisting of up to eight subunits (*10*). They are initially loosely packed but can become more ordered over time. To characterize the perforin conformation in these assemblies, we used a TMH1-lock mutant of perforin (A144C-W373C), in which TMH1 is tethered to the core of the MACPF domain (*10*). This prevents the refolding of either TMH region into a β-hairpin and thereby completely blocks membrane insertion. The engineered disulfide bond in this mutant tethers the TMH1 region to a conserved MACPF α helix. Perforin prepores are less ordered than mature pores and could not be isolated from liposomes, so it was necessary to use cryo-tomography to study the prepores on liposomes. For prepore formation, liposomes containing 10% biotinylated lipids were immobilized on functionalized EM grids containing streptavidin to prevent liposome aggregation upon addition of perforin in the presence of Ca^{2+}.

Multiple perforin assemblies, mainly incomplete rings, were clearly visible on the surface of the liposomes (Fig. 4A). The height of these assemblies, 10.5 to 11 nm, agrees well with prepore height measurements by atomic force microscopy (*10*). The shape of the perforin molecule crystal structure is easily recognizable in the density sections, with the narrower Ca^{2+}-binding C2 domain docked on the membrane surface (Fig. 4B). Because of the small number and heterogeneity of the prepores, subtomogram averaging was not feasible and the limited resolution of the tomograms did not allow us to determine conformational changes at the domain level. Nevertheless, the crystal structure of the soluble perforin monomer could be manually docked into the prepore density, qualitatively demonstrating that no major conformational change is required for prepore formation (Fig. 4C).

DISCUSSION

In this study, we have used single-particle cryo-EM to determine the structure of membrane-inserted perforin pore at near-atomic resolution. In combination with a previously solved crystal structure of the soluble perforin monomer, this work describes the conformational changes that lead to membrane insertion of perforin.

Perforin is the key effector of cytotoxicity inflicted by activated $CD8^+$ T cells and NK cells, mediated by its ability to form transmembrane pores that deliver granzymes to the target cell cytosol. Various human disorders have been associated with dysregulated biosynthesis or mutations that affect the perforin structure. These mutations are spread throughout the MACPF and C2 domains of the protein (*14*, *54*) (figs. S4 and S5, all numbering used in this section corresponds to the human perforin sequence for comparison with clinical data). The most serious of these disorders is type 2 FHL, which is specifically associated with loss of perforin expression or function (*14*). Current treatment of FHL includes chemotherapy, immunosuppression with high-dose corticosteroids, and antibiotic and/or antiviral drugs to address any potential infectious trigger. There is no treatment available to date that aims to restore perforin function or its delivery into the immunological synapse, although even mild changes in perforin activity might contribute to immune dysregulation (*55*). The structure of the inserted form of perforin provides insight into the mechanism of pore formation and suggests how some FHL-causing mutations affect protein structure and function.

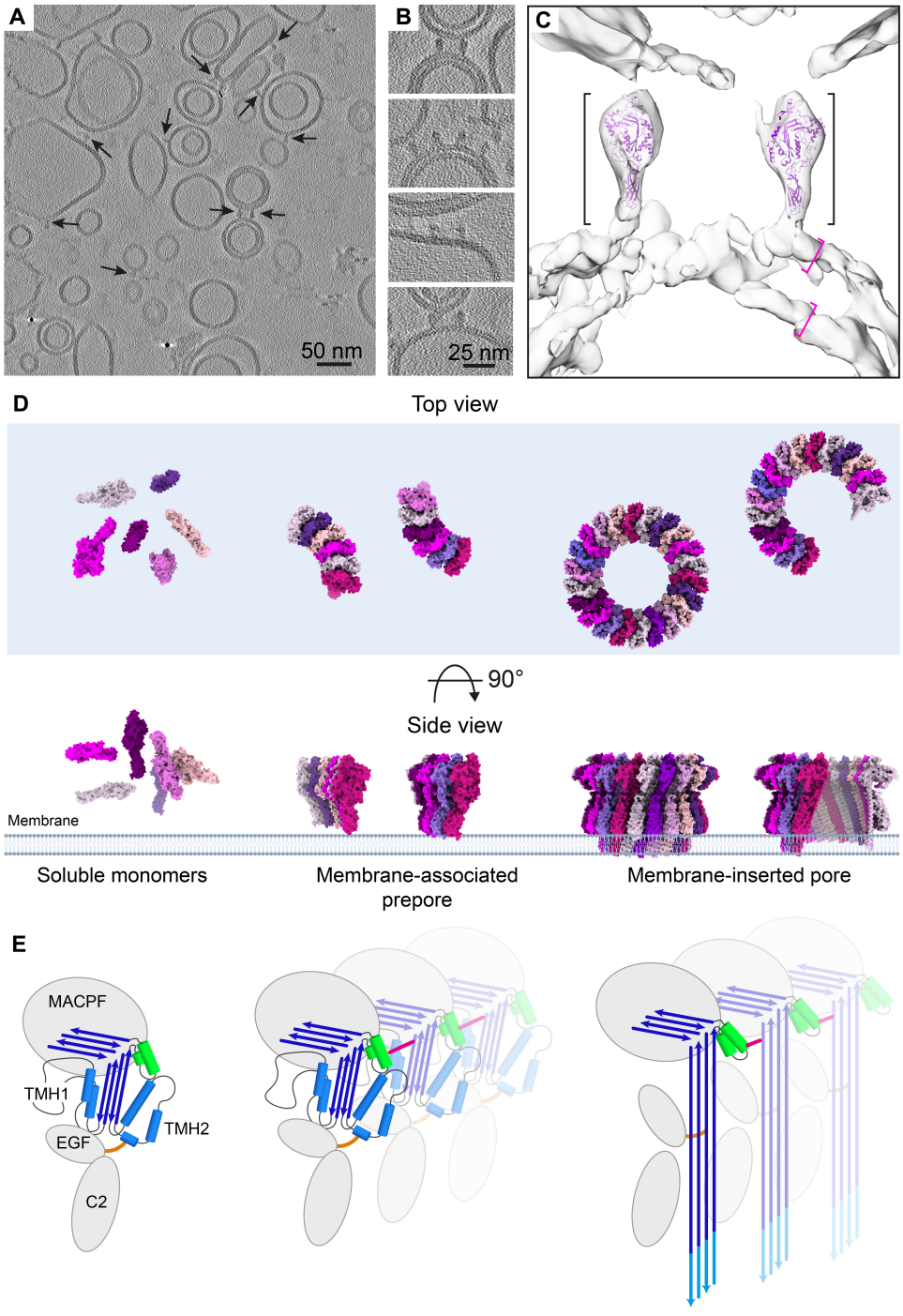

Fig. 4. Cryo-tomography of perforin prepores. (**A**) Overview of a typical cryotomogram of liposomes with attached perforin prepores. Prepore assemblies are highlighted with arrows. (**B**) Close-up view of prepores attached to the lipid bilayers. (**C**) Manual docking of soluble perforin monomer (purple, PDB code 3NSJ) into the 3D volume of a perforin prepore on a double-shelled liposome. Density corresponding to the prepore is indicated by black brackets, and density corresponding to each membrane bilayer is marked by pink brackets. (**D**) Model of the molecular assemblies during pore formation. (**E**) Schematic representation of the conformational changes and assembly interactions. The HTH region is shown in green, the bond between the HTH and a neighboring β strand in pink, disulfide bond between EGF domain and TMH2 in orange, the initial β sheets in blue, and the transmembrane region in cyan.

The MACPF/CDC family includes hundreds of diverse proteins, but few have been extensively studied and structural information is available for even fewer. Medium-resolution structures of the pneumolysin pore and the MAC complex in its inserted form have been determined by cryo-EM (*31*, *32*, *56*). The MACPF domains of these proteins are structurally conserved and contain a signature motif (Y/W)G(T/S)H(F/Y)X_6GG, but otherwise share very little sequence similarity and contain diverse auxiliary domains. Some of

Table 1. Cryo-EM data collection, refinement, and validation statistics.

Data collection and processing		
Voltage	300	
Electron exposure (e^{-}/Å^2)	49.6	
Defocus range (μm)	1.5–3.3	
Nominal magnification	105,000×	
Pixel size (Å)	1.38	
Initial particle images (no.)	1,062,243	
Final particle images (no.)	229,789	
Map resolution (Å) (FSC = 0.143)	4.0	
Map resolution range (Å)	3.9–7.3	
Model refinement		
	Monomer	Trimer
Initial model used (PDB code)	3nsj	
Model resolution (Å) (FSC = 0.5)	7.4	6.7
Model resolution (Å) (FSC = 0.143)	4.0	4.0
Map sharpening B factor (Å^2)	−95	−95
Model composition		
Nonhydrogen atoms	4,040	12,120
Protein residues	509	1,527
Ligands		
Ca	3	9
NAG	1	3
B factors (Å^2)		
Protein	129.8	134.6
Ligand	188.8	182.4
RMSDs		
Bond lengths (Å)	0.27	0.28
Bond angles (°)	0.55	0.61
Validation		
MolProbity score	2.0 (77th percentile*)	2.2
Clashscore	12.4 (67th percentile*)	21.2
Poor rotamers (%)	0	0
Ramachandran plot		
Favored (%)	94	94
Allowed (%)	6	6
Disallowed (%)	0	0

*100th is the best among the structures; 0th is the worst.

the key structural features described here are broadly conserved in the MACPF/CDC superfamily (Fig. 3) (*32*, *36*, *52*, *56*). In the soluble forms, the most conserved feature is the MACPF topology, with the central, bent β sheet flanked by the largely helical bundles TMH1 and TMH2. In addition, the membrane-docking domain often has a β sandwich or C2 fold. Also broadly conserved is the HTH motif, located at the crucial bend in the central β sheet, which tends to straighten out in the pore forms as the TMH regions are released to refold into the β barrel. A regulatory role for the HTH was postulated by Lukoyanova *et al.* (*52*) in a comparison of prepore and pore structures of the fungal MACPF protein pleurotolysin, supported by the map of a poly-C9 pore (*57*). Subsequent higher-resolution studies have provided more detail on the HTH, its movements and surface charges, in the MAC (*32*) and in the CDC pneumolysin (*56*). However, the connection between MACPF and membrane-docking domains is more variable. CDCs have a thin connecting β domain that collapses, allowing its shorter TMHs to reach the membrane (*10*). Perforin-2 has a unique P2 domain linker between its EGF domain and the membrane-docking region (*35*).

The perforin domains play distinct roles: The MACPF domain is responsible for oligomerization and membrane insertion, the C2 domain binds Ca^{2+} ions and docks the molecule onto the membrane, while the EGF domain provides flexibility, links the MACPF and C2 domains, and is tethered to TMH2. Canonical EGF domains have diverse functions, including extracellular and intracellular signaling, ligand recognition, and mediating protein interactions. MAC proteins also contain EGF domains, but their position relative to the MACPF domain is different from the one in perforin and they lack a disulfide bond linking them to the TMH2 domain. However, the EGF domains may play a regulatory role in both perforin and MAC.

Soluble perforin is monomeric (*53*), whereas in the presence of a lipid bilayer, perforin molecules dock onto the membrane surface via the Ca^{2+} binding sites at the base of the C2 domain and then oligomerize. Leung *et al.* (*10*) identified two possible types of perforin prepores, early and late prepores, with more compact subunit packing at the later stage. Both types of prepore formed shorter segments, with 2× to 5× fewer subunits than the pores. Using a mutant with a disulfide bond introduced to lock one of the TMH domains to a neighboring region, pore formation could be induced by addition of reducing agent to release the TMH regions. Prepore oligomerization on the membrane is not reversible (*10*), suggesting that oligomerization involves a conformational change preceding β-barrel formation and membrane insertion. We speculate that the newly identified interaction between the HTH motif of one molecule and a β strand of the adjacent subunit forms at the prepore stage and might stabilize the prepore and promote further assembly (Fig. 4D). This hypothesis is supported by the recently solved structure of the Intermedilysin prepore (*58*), which shows that the HTH motif assembles before membrane insertion. Displacement of the HTH domain away from the core of the MACPF domain in perforin is accompanied by formation of a new intermolecular interaction between the HTH motif and R298, which, in turn, slightly unbends the central β sheet, releasing the TMH2 helices for unfolding and conversion into β hairpins. The HTH motif is located adjacent to the bend in the central β sheet, flanked by two glycine residues that are conserved throughout the MACPF/CDC superfamily, allowing for flexibility at the bend in the β sheet. Partial straightening of this bend is crucial to the MACPF/CDC conformational change. Our discovery of an intersubunit contact involving this region is highly

significant, since it links triggering of the conformational change to oligomerization (Fig. 4E).

This study provides important insights into the structure of the clinically significant protein perforin in its membrane inserted form, as well as explaining the mode of action of some pathogenic mutations. Furthermore, our observations help us to understand the mechanism of pore formation by MACPF proteins and suggest the order of conformational changes required for membrane insertion.

METHODS

Protein expression and sample preparation for EM analysis

WT and TMH1-lock mutant (A144C-W373C) perforin were expressed in a baculovirus/insect cell system and purified from the supernatant as described by Voskoboinik and colleagues (*10*, *38*). PC lipid (100 μl) dissolved in chloroform at 10 mg/ml (Avanti Polar Lipids, USA) was dried under nitrogen gas and resuspended in 1 ml of buffer containing 20 mM Hepes at pH 7.5, 150 mM NaCl, and 5 mM $CaCl_2$. Rehydrated lipid solution was sonicated in a water bath at 40°C for 10 min followed by flash freezing in liquid nitrogen. Thawing and sonication followed by flash freezing were repeated three times, yielding a solution of large multilamellar vesicles, which was forced through a polycarbonate filter with 80-nm pore membrane around 20 times using the Avanti mini-extruder at 40°C. The resulting liposome suspension was stored at 4°C and used within 48 hours.

Perforin pores were assembled on liposomes by incubating 5 μl of the liposome solution with 15 μl of purified protein at a concentration of 200 to 300 ng/ml for 15 min at 37°C. For the preparation of perforin pore complexes, the proteoliposomes were solubilized at a final concentration of 1% Triton X-100 at room temperature overnight. Solubilized pores were stored at 4°C and used within 48 hours.

Negative-stain and cryo-EM of perforin pores

For negative-stain EM, 3 μl of solubilized perforin pores was applied onto a continuous carbon transmission electron microscopy (TEM) grid (Electron Microscope Sciences, USA) freshly negatively glow-discharged using PELCO easiGlow (Ted Pella, USA) and stained with 2% (w/v) uranyl acetate. Negatively stained specimens were examined with a T12 EM (FEI, The Netherlands) operated at an acceleration voltage of 120 keV. Images were recorded with a 4kx4k UltraScan charge-coupled device camera (Gatan, USA) at a nominal magnification of 25,000 to 45,000 and ~1.0- to 2.0-μm underfocus.

For cryo-EM, UltrAuFoil R 2.0/2.0 grids (Quantifoil, Germany) were negatively glow-discharged using PELCO easiGlow and coated with graphene oxide as described by Cheng *et al.* (*59*). To increase particle concentration, 3 μl of the sample was applied twice with a 30-s interval and 0.5-s blotting before the second application inside the chamber of Vitrobot Mark IV (Thermo Fisher Scientific, USA) at 4°C and 92% humidity. Samples were vitrified in liquid ethane. Cryo-EM data were collected at the ISMB Birkbeck EM facility using a Titan Krios microscope (Thermo Fisher Scientific, USA) operated at 300 keV and equipped with a BioQuantum energy filter (Gatan, USA) using a slit width of 20 eV. The images were collected with a post-GIF K3 direct electron detector (Gatan, USA) operated in super-resolution mode, at a magnification of 64,000, corresponding to a physical pixel size of 1.34 Å. The dose rate was set to 16 e^-/pixel per second, and a total dose of 49.6 $e^-/Å^2$ was fractionated over 50 frames. Data were collected using EPU software (Thermo Fisher Scientific, USA) with a defocus range of 1.5 to 3.3 μm. A total of 19,627 movies were collected. To mitigate preferred orientation of perforin pores on the continuous substrate, the microscope stage was tilted −30° during data collection.

Image processing

Electron micrograph movie frames were aligned by MotionCor2 (*60*) using the RELION v3.1 implementation (*61*). Super-resolution movies were additionally down-sampled by a factor of 2, applied by Fourier binning within MotionCor2. All aligned movie frames were subsequently averaged into dose-weighted and nonweighted sums for further processing. Contrast transfer function (CTF) estimation of whole non–dose-weighted micrographs was initially performed with CTFFIND4 (*62*).

Particle coordinates were determined using Gautomatch (developed by K. Zhang; https://www2.mrc-lmb.cam.ac.uk/research/locally-developed-software/zhang-software/), and particles were extracted with a box size of 320 pixels using RELION. Extracted particles were imported into cryoSPARC v2 (*63*) for five rounds of 2D classification. Particles corresponding to 2D class averages showing clear features and having similar diameter were selected, and all further processing was performed in RELION v3.1 unless otherwise stated (fig. S2).

Particles were subjected to two rounds of 3D classification followed by one round of consensus 3D refinement. Particles corresponding to the class showing the most defined features and the most complete ring were selected for further processing. This was followed by two rounds of per-particle CTF estimation and further 3D refinement. These alignments served as the starting point for tracking beam-induced movement of individual particles, which was corrected using particle polishing in RELION. The final subset of particles included images of perforin pores containing mainly 22 monomers, but because of pore flexibility, the structure was refined without imposing symmetry; this yielded a reconstruction with 7.1-Å global resolution, estimated using the gold standard Fourier shell correlation (FSC) with a 0.143 threshold. Subsequently, symmetry expansion was implemented such that each particle was assigned 22 orientations that corresponded to its symmetry-related views. These particles were then subjected to one round of 3D refinement with only local angular searches, and local resolution estimation of the final map had been performed. A mask was prepared to only include five monomers of perforin that were best defined, while the rest of the pore was subtracted from the original images. Focused 3D refinement was performed to improve the resolution of this five-subunit wedge of the perforin ring; this was followed by another round of 3D refinement with only local angular searches, yielding 4.1-Å resolution. To limit anisotropy of the map, 229,789 particles out of about 5,000,000 symmetry-expanded copies were selected for the final refinement using rlnMaxValueProbDistribution criteria (*64*); the remaining particles, corresponding to overrepresented views, were excluded. This procedure reduced the average resolution of the map from 4.1 to 4.5 Å but improved the definition of structural features. A calibrated pixel size of 1.34 Å was applied for RELION postprocessing, yielding a global resolution of 4.0 Å, determined by gold standard FSC with 0.143 threshold (fig. S1C). Local resolution was estimated in RELION using a windowed $FSC_{0.143}$. Details of data collection are presented in Table 1.

Model building and analysis

For model building, the final map was modified using Phenix Resolve software (*65*). The initial model was generated in Coot (*66*)

using the previously determined crystal structure of a soluble perforin monomer (*34*) and an atomic model of MAC C9 protein built into a cryo-EM map (*32*). Model building was performed using a combination of Flex-EM (with disulfide and secondary structure restraints) (*67*), Coot, and real-space refinement in Phenix (*68*). The resulting fit of the EGF domain did not correlate well with the map, although the local resolution of the map is ~4.3 Å. Therefore, the EGF domain was corrected by manual tracing in Coot where possible, taking into account disulfide bonds, and refined in Phenix. About 10 residues of the EGF domain could not be unambiguously built and were omitted from the final model.

Initially, the perforin model was refined as a trimer to account for intermolecular interactions. In the last few rounds of refinement, the model was refined as a monomer, which was deposited in the Protein Data Bank (PDB) with accession number 7PAG. Model validation was performed using MolProbity (*69*) and the CCP-EM software suite (*70*). Details of refinement and validation statistics for both a monomer and a trimer of perforin are included in Table 1. The pore model with 22 subunits was generated in UCSF Chimera (*71*). Density maps and models were visualized, and figures were drawn in UCSF ChimeraX (*72*). Coulombic potentials of interaction interfaces were calculated and visualized in UCSF Chimera.

Cryo–electron tomography of perforin prepores

Liposomes were prepared as described above using PC, cholesterol, and 1,2-dipalmitoyl-sn-glycero-3-phosphoethanolamine-*N*-(biotinyl) (Biotinyl PE) at a 6:3:1 molar ratio. Liposome concentration was checked by negative-stain EM before sample preparation. To prevent liposome aggregation upon prepore formation, we used C-SMART Streptavidin BioGrids (Dunes Sciences Inc., USA) with a thin layer of continuous carbon derivatized with streptavidin over a lacey carbon substrate. Streptavidin BioGrids were first rinsed with buffer containing 20 mM Hepes at pH 7.5, 150 mM NaCl, and 5 mM $CaCl_2$ by floating on a droplet, then incubated with diluted liposomes inside a humid chamber at 37°C for 10 to 20 min, and rinsed on a buffer droplet again without blotting. Then, 3 µl of TMH1-lock mutant (A144C-W373C) perforin diluted in the same buffer was added directly onto a grid at an approximate protein to lipid molar ratio of 1:10,000. The grid was then transferred into the chamber of Vitrobot Mark IV and, after 5- to 10-min incubation at 37°C and 90% humidity, blotted and vitrified in liquid ethane. Immediately before blotting, 1 µl of 6-nm Protein A gold fiducials (Electron Microscope Sciences, USA) diluted five times with the above buffer was added directly onto the grid.

Tilt series were collected at the eBIC National facility using a Titan Krios microscope operated at 300 keV with a post-GIF K2 Summit direct electron detector (Gatan, USA) operating in counting mode, at a nominal magnification of 81,000, corresponding to a pixel size of 1.77 Å. The dose rate was set to 6.2 e^-/pixel per second. Tomo 3 software (Thermo Fisher Scientific, USA) was used to collect tilt series between −45° and 45° using a linear tilt scheme with 3° increments starting at 0° tilt with tracking before and after. A total exposure of ~50 $e^-/Å^2$ was fractionated over 93 frames with 1.6 $e^-/Å^2$ dose per tilt. An energy slit with a 20-eV width was used during data collection. A volta phase plate (VPP) was used to enhance the contrast and data collected with a nominal defocus range from 60 to 120 nm. The VPP was advanced to a new position for every tilt series, with 40-s activation time and total dose on the VPP ~50 nC.

MotionCor2 v1.0.5 (*60*) was used for subframe alignment and dose weighting. Tilt series were aligned and reconstructed by weighted back-projection using IMOD/etomo (*73*).

SUPPLEMENTARY MATERIALS

Supplementary material for this article is available at https://science.org/doi/10.1126/sciadv.abk3147

View/request a protocol for this paper from *Bio-protocol*.

REFERENCES AND NOTES

1. B. V. Kumar, T. J. Connors, D. L. Farber, Human T cell development, localization, and function throughout life. *Immunity* **48**, 202–213 (2018).
2. A. M. Abel, C. Yang, M. S. Thakar, S. Malarkannan, Natural killer cells: Development, maturation, and clinical utilization. *Front. Immunol.* **9**, 1869 (2018).
3. E. R. Podack, J. D. E. Young, Z. A. Cohn, Isolation and biochemical and functional characterization of perforin 1 from cytolytic T-cell granules. *Proc. Natl. Acad. Sci. U.S.A.* **82**, 8629–8633 (1985).
4. J. D. Young, Z. A. Cohn, E. R. Podack, The ninth component of complement and the pore-forming protein (perforin 1) from cytotoxic T cells: Structural, immunological, and functional similarities. *Science* **233**, 184–190 (1986).
5. J. D. Young, H. Hengartner, E. R. Podack, Z. A. Cohn, Purification and characterization of a cytolytic pore-forming protein from granules of cloned lymphocytes with natural killer activity. *Cell* **44**, 849–859 (1986).
6. O. Krähenbühl, C. Rey, D. Jenne, A. Lanzavecchia, P. Groscurth, S. Carrel, J. Tschopp, Characterization of granzymes A and B isolated from granules of cloned human cytotoxic T lymphocyte. *J. Immunol.* **141**, 3471–3477 (1988).
7. J. R. Yannelli, J. A. Sullivan, G. L. Mandell, V. H. Engelhard, Reorientation and fusion of cytotoxic T lymphocyte granules after interaction with target cells as determined by high resolution cinemicrography. *J. Immunol.* **136**, 377–382 (1986).
8. H. Nakajima, H. L. Park, P. A. Henkart, Synergistic roles of granzymes A and B in mediating target cell death by rat basophilic leukemia mast cell tumors also expressing cytolysin/perforin. *J. Exp. Med.* **181**, 1037–1046 (1995).
9. L. Shi, C. M. Kam, J. C. Powers, R. Aebersold, A. H. Greenberg, Purification of three cytotoxic lymphocyte granule serine proteases that induce apoptosis through distinct substrate and target cell interactions. *J. Exp. Med.* **176**, 1521–1529 (1992).
10. C. Leung, A. W. Hodel, A. J. Brennan, N. Lukoyanova, S. Tran, C. M. House, S. C. Kondos, J. C. Whisstock, M. A. Dunstone, J. A. Trapani, I. Voskoboinik, H. R. Saibil, B. W. Hoogenboom, Real-time visualization of perforin nanopore assembly. *Nat. Nanotechnol.* **12**, 467–473 (2017).
11. X. Liu, J. Lieberman, Knocking 'em dead: Pore-forming proteins in immune defense. *Annu. Rev. Immunol.* **38**, 455–485 (2020).
12. G. De Saint Basile, G. Ménasché, A. Fischer, Molecular mechanisms of biogenesis and exocytosis of cytotoxic granules. *Nat. Rev. Immunol.* **10**, 568–579 (2010).
13. C. Gholam, S. Grigoriadou, K. C. Gilmour, H. B. Gaspar, Familial haemophagocytic lymphohistiocytosis: Advances in the genetic basis, diagnosis and management. *Clin. Exp. Immunol.* **163**, 271–283 (2011).
14. I. Voskoboinik, J. A. Trapani, Perforinopathy: A spectrum of human immune disease caused by defective perforin delivery or function. *Front. Immunol.* **4**, 441 (2013).
15. J. Chia, P. Y. Kim, J. C. Whisstock, M. A. Dunstone, J. A. Trapani, I. Voskoboinik, Temperature sensitivity of human perforin mutants unmasks subtotal loss of cytotoxicity, delayed FHL, and a predisposition to cancer. *Proc. Natl. Acad. Sci. U.S.A.* **106**, 9809–9814 (2009).
16. R. Clementi, F. Locatelli, L. Dupré, A. Garaventa, L. Emmi, M. Bregni, G. Cefalo, A. Moretta, C. Danesino, M. Comis, A. Pession, U. Ramenghi, R. Maccario, M. Aricò, M. G. Roncarolo, A proportion of patients with lymphoma may harbor mutations of the perforin gene. *Blood* **105**, 4424–4428 (2005).
17. A. J. Brennan, J. Chia, J. A. Trapani, I. Voskoboinik, Perforin deficiency and susceptibility to cancer. *Cell Death Differ.* **17**, 607–615 (2010).
18. J. A. Trapani, K. Y. T. Thia, M. Andrews, I. D. Davis, C. Gedye, P. Parente, S. Svobodova, J. Chia, K. Browne, I. G. Campbell, W. A. Phillips, I. Voskoboinik, J. S. Cebon, Human perforin mutations and susceptibility to multiple primary cancers. *Oncoimmunology* **2**, e24185 (2013).
19. C. F. Reboul, J. C. Whisstock, M. A. Dunstone, Giant MACPF/CDC pore forming toxins: A class of their own. *Biochim. Biophys. Acta Biomembr.* **1858**, 475–486 (2016).
20. Y. Shinkai, K. Takio, K. Okumura, Homology of perforin to the ninth component of complement (C9). *Nature* **334**, 525–527 (1988).
21. N. Lukoyanova, B. W. Hoogenboom, H. R. Saibil, The membrane attack complex, perforin and cholesterol-dependent cytolysin superfamily of pore-forming proteins. *J. Cell Sci.* **129**, 2125–2133 (2016).

22. H. Nagai, N. Oshiro, K. Takuwa-Kuroda, S. Iwanaga, M. Nozaki, T. Nakajima, Novel proteinaceous toxins from the nematocyst venom of the Okinawan sea anemone Phyllodiscus semoni Kwietniewski. *Biochem. Biophys. Res. Commun.* **294**, 760–763 (2002).
23. J. D. Young, L. G. Leong, C. C. Liu, A. Damiano, Z. A. Cohn, Extracellular release of lymphocyte cytolytic pore-forming protein (perforin) after ionophore stimulation. *Proc. Natl. Acad. Sci. U.S.A.* **83**, 5668–5672 (1986).
24. J. R. Martin, A. Raibaud, R. Ollo, Terminal pattern elements in *Drosophila* embryo induced by the *torso-like* protein. *Nature* **367**, 741–745 (1994).
25. S. Garg, S. Agarwal, S. Kumar, S. Shams Yazdani, C. E. Chitnis, S. Singh, Calcium-dependent permeabilization of erythrocytes by a perforin-like protein during egress of malaria parasites. *Nat. Commun.* **4**, 1736 (2013).
26. E. Mulvihill, L. Sborgi, S. A. Mari, M. Pfreundschuh, S. Hiller, D. J. Müller, Mechanism of membrane pore formation by human gasdermin-D. *EMBO J.* **37**, e98321 (2018).
27. O. Shatursky, A. P. Heuck, L. A. Shepard, J. Rossjohn, M. W. Parker, A. E. Johnson, R. K. Tweten, The mechanism of membrane insertion for a cholesterol-dependent cytolysin: A novel paradigm for pore-forming toxins. *Cell* **99**, 293–299 (1999).
28. L. A. Shepard, O. Shatursky, A. E. Johnson, R. K. Tweten, The mechanism of pore assembly for a cholesterol-dependent cytolysin: Formation of a large prepore complex precedes the insertion of the transmembrane β-hairpins. *Biochemistry* **39**, 10284–10293 (2000).
29. S. Bhakdi, J. Tranum-Jensen, A. Sziegoleit, Mechanism of membrane damage by streptolysin-O. *Infect. Immun.* **47**, 52–60 (1985).
30. T. Praper, A. Sonnen, G. Viero, A. Kladnik, C. J. Froelich, G. Anderluh, M. Dalla Serra, R. J. C. Gilbert, Human perforin employs different avenues to damage membranes. *J. Biol. Chem.* **286**, 2946–2955 (2011).
31. C. Leung, N. V. Dudkina, N. Lukoyanova, A. W. Hodel, I. Farabella, A. P. Pandurangan, N. Jahan, M. Pires Damaso, D. Osmanović, C. F. Reboul, M. A. Dunstone, P. W. Andrew, R. Lonnen, M. Topf, H. R. Saibil, B. W. Hoogenboom, Stepwise visualization of membrane pore formation by suilysin, a bacterial cholesterol-dependent cytolysin. *eLife* **3**, e04247 (2014).
32. A. Menny, M. Serna, C. M. Boyd, S. Gardner, A. P. Joseph, B. P. Morgan, M. Topf, N. J. Brooks, D. Bubeck, CryoEM reveals how the complement membrane attack complex ruptures lipid bilayers. *Nat. Commun.* **9**, 5316 (2018).
33. E. S. Parsons, G. J. Stanley, A. L. B. Pyne, A. W. Hodel, A. P. Nievergelt, A. Menny, A. R. Yon, A. Rowley, R. P. Richter, G. E. Fantner, D. Bubeck, B. W. Hoogenboom, Single-molecule kinetics of pore assembly by the membrane attack complex. *Nat. Commun.* **10**, 2066 (2019).
34. R. H. P. Law, N. Lukoyanova, I. Voskoboinik, T. T. Caradoc-Davies, K. Baran, M. A. Dunstone, M. E. D'Angelo, E. V. Orlova, F. Coulibaly, S. Verschoor, K. A. Browne, A. Ciccone, M. J. Kuiper, P. I. Bird, J. A. Trapani, H. R. Saibil, J. C. Whisstock, The structural basis for membrane binding and pore formation by lymphocyte perforin. *Nature* **468**, 447–451 (2010).
35. T. Ni, F. Jiao, X. Yu, S. Aden, L. Ginger, S. I. Williams, F. Bai, V. Pražák, D. Karia, P. Stansfeld, P. Zhang, G. Munson, G. Anderluh, S. Scheuring, R. J. C. Gilbert, Structure and mechanism of bactericidal mammalian perforin-2, an ancient agent of innate immunity. *Sci. Adv.* **6**, eaax8286 (2020).
36. S. S. Pang, C. Bayly-Jones, M. Radjainia, B. A. Spicer, R. H. P. Law, A. W. Hodel, E. S. Parsons, S. M. Ekkel, P. J. Conroy, G. Ramm, H. Venugopal, P. I. Bird, B. W. Hoogenboom, I. Voskoboinik, Y. Gambin, E. Sierecki, M. A. Dunstone, J. C. Whisstock, The cryo-EM structure of the acid activatable pore-forming immune effector macrophage-expressed gene 1. *Nat. Commun.* **10**, 4288 (2019).
37. J. Ruan, S. Xia, X. Liu, J. Lieberman, H. Wu, Cryo-EM structure of the gasdermin A3 membrane pore. *Nature* **557**, 62–67 (2018).
38. I. Voskoboinik, M. C. Thia, A. De Bono, K. Browne, E. Cretney, J. T. Jackson, P. K. Darcy, S. M. Jane, M. J. Smyth, J. A. Trapani, The functional basis for hemophagocytic lymphohistiocytosis in a patient with co-inherited missense mutations in the perforin (PFN1) gene. *J. Exp. Med.* **200**, 811–816 (2004).
39. R. Uellner, M. J. Zvelebil, J. Hopkins, J. Jones, L. K. MacDougall, B. P. Morgan, E. Podack, M. D. Waterfield, G. M. Griffiths, Perforin is activated by a proteolytic cleavage during biosynthesis which reveals a phospholipid-binding C2 domain. *EMBO J.* **16**, 7287–7296 (1997).
40. I. G. House, C. M. House, A. J. Brennan, O. Gilan, M. A. Dawson, J. C. Whisstock, R. H. Law, J. A. Trapani, I. Voskoboinik, Regulation of perforin activation and pre-synaptic toxicity through C-terminal glycosylation. *EMBO Rep.* **18**, 1775–1785 (2017).
41. A. J. Brennan, J. Chia, K. A. Browne, A. Ciccone, S. Ellis, J. A. Lopez, O. Susanto, S. Verschoor, H. Yagita, J. C. Whisstock, J. A. Trapani, I. Voskoboinik, Protection from endogenous perforin: Glycans and the C terminus regulate exocytic trafficking in cytotoxic lymphocytes. *Immunity* **34**, 879–892 (2011).
42. A. G. Murzin, New protein folds. *Curr. Opin. Struct. Biol.* **4**, 441–449 (1994).
43. C. F. Reboul, K. Mahmood, J. C. Whisstock, M. A. Dunstone, Predicting giant transmembrane β-barrel architecture. *Bioinformatics* **28**, 1299–1302 (2012).
44. S. E. Stewart, S. C. Kondos, A. Y. Matthews, M. E. D'Angelo, M. A. Dunstone, J. C. Whisstock, J. A. Trapani, P. I. Bird, The perforin pore facilitates the delivery of cationic cargos. *J. Biol. Chem.* **289**, 9172–9181 (2014).
45. I. Walev, S. C. Bhakdi, F. Hofmann, N. Djonder, A. Valeva, K. Aktories, S. Bhakdi, Delivery of proteins into living cells by reversible membrane permeabilization with streptolysin-O. *Proc. Natl. Acad. Sci. U.S.A.* **98**, 3185–3190 (2001).
46. S. Xia, Z. Zhang, V. G. Magupalli, J. L. Pablo, Y. Dong, S. M. Vora, L. Wang, T.-M. Fu, M. P. Jacobson, A. Greka, J. Lieberman, J. Ruan, H. Wu, Gasdermin D pore structure reveals preferential release of mature interleukin-1. *Nature* **593**, 607–611 (2021).
47. S. Molleran Lee, J. Villanueva, J. Sumegi, K. Zhang, K. Kogawa, J. Davis, A. H. Filipovich, Characterisation of diverse PRF1 mutations leading to decreased natural killer cell activity in North American families with haemophagocytic lymphohistiocytosis. *J. Med. Genet.* **41**, 137–144 (2004).
48. M. A. Wouters, I. Rigoutsos, C. K. Chu, L. L. Feng, D. B. Sparrow, S. L. Dunwoodie, Evolution of distinct EGF domains with specific functions. *Protein Sci.* **14**, 1091–1103 (2005).
49. R. C. Willenbring, A. J. Johnson, Finding a balance between protection and pathology: The dual role of perforin in human disease. *Int. J. Mol. Sci.* **18**, 1608 (2017).
50. I. Voskoboinik, M. C. Thia, J. A. Trapani, A functional analysis of the putative polymorphisms A91V and N252S and 22 missense perforin mutations associated with familial hemophagocytic lymphohistiocytosis. *Blood* **105**, 4700–4706 (2005).
51. K. A. Risma, R. W. Frayer, A. H. Filipovich, J. Sumegi, Aberrant maturation of mutant perforin underlies the clinical diversity of hemophagocytic lymphohistiocytosis. *J. Clin. Invest.* **116**, 182–192 (2006).
52. N. Lukoyanova, S. C. Kondos, I. Farabella, R. H. P. Law, C. F. Reboul, T. T. Caradoc-Davies, B. A. Spicer, O. Kleifeld, D. A. K. Traore, S. M. Ekkel, I. Voskoboinik, J. A. Trapani, T. Hatfaludi, K. Oliver, E. M. Hotze, R. K. Tweten, J. C. Whisstock, M. Topf, H. R. Saibil, M. A. Dunstone, Conformational changes during pore formation by the perforin-related protein pleurotolysin. *PLOS Biol.* **13**, e1002049 (2015).
53. K. Baran, M. Dunstone, J. Chia, A. Ciccone, K. A. Browne, C. J. P. Clarke, N. Lukoyanova, H. Saibil, J. C. Whisstock, I. Voskoboinik, J. A. Trapani, The molecular basis for perforin oligomerization and transmembrane pore assembly. *Immunity* **30**, 684–695 (2009).
54. I. Voskoboinik, J. C. Whisstock, J. A. Trapani, Perforin and granzymes: Function, dysfunction and human pathology. *Nat. Rev. Immunol.* **15**, 388–400 (2015).
55. S. E. Stepp, R. Dufourcq-Lagelouse, F. Le Deist, S. Bhawan, S. Certain, P. A. Mathew, J. I. Henter, M. Bennett, A. Fischer, G. De Saint Basile, V. Kumar, Perforin gene defects in familial hemophagocytic lymphohistiocytosis. *Science* **286**, 1957–1959 (1999).
56. K. van Pee, A. Neuhaus, E. D'Imprima, D. J. Mills, W. Kühlbrandt, Ö. Yildiz, CryoEM structures of membrane pore and prepore complex reveal cytolytic mechanism of pneumolysin. *eLife* **6**, e23644 (2017).
57. N. V. Dudkina, B. A. Spicer, C. F. Reboul, P. J. Conroy, N. Lukoyanova, H. Elmlund, R. H. P. Law, S. M. Ekkel, S. C. Kondos, R. J. A. Goode, G. Ramm, J. C. Whisstock, H. R. Saibil, M. A. Dunstone, Structure of the poly-C9 component of the complement membrane attack complex. *Nat. Commun.* **7**, (2016).
58. N. R. Shah, T. B. Voisin, E. S. Parsons, C. M. Boyd, B. W. Hoogenboom, D. Bubeck, Structural basis for tuning activity and membrane specificity of bacterial cytolysins. *Nat. Commun.* **11**, 5818 (2020).
59. K. Cheng, M. Wilkinson, Y. Chaban, D. B. Wigley, A conformational switch in response to Chi converts RecBCD from phage destruction to DNA repair. *Nat. Struct. Mol. Biol.* **27**, 71–77 (2020).
60. S. Q. Zheng, E. Palovcak, J. P. Armache, K. A. Verba, Y. Cheng, D. A. Agard, MotionCor2: Anisotropic correction of beam-induced motion for improved cryo-electron microscopy. *Nat. Methods* **14**, 331–332 (2017).
61. J. Zivanov, T. Nakane, B. O. Forsberg, D. Kimanius, W. J. H. Hagen, E. Lindahl, S. H. W. Scheres, New tools for automated high-resolution cryo-EM structure determination in RELION-3. *eLife* **7**, (2018).
62. A. Rohou, N. Grigorieff, CTFFIND4: Fast and accurate defocus estimation from electron micrographs. *J. Struct. Biol.* **192**, 216–221 (2015).
63. A. Punjani, J. L. Rubinstein, D. J. Fleet, M. A. Brubaker, CryoSPARC: Algorithms for rapid unsupervised cryo-EM structure determination. *Nat. Methods* **14**, 290–296 (2017).
64. A. Meir, K. Macé, N. Lukoyanova, D. Chetrit, M. K. Hospenthal, A. Redzej, C. Roy, G. Waksman, Mechanism of effector capture and delivery by the type IV secretion system from *Legionella pneumophila*. *Nat. Commun.* **11**, 2864 (2020).
65. T. C. Terwilliger, S. J. Ludtke, R. J. Read, P. D. Adams, P. V. Afonine, Improvement of cryo-EM maps by density modification. *Nat. Methods* **17**, 923–927 (2020).
66. P. Emsley, B. Lohkamp, W. G. Scott, K. Cowtan, Features and development of Coot. *Acta Crystallogr. Sect. D Biol. Crystallogr.* **66**, 486–501 (2010).
67. M. Topf, K. Lasker, B. Webb, H. Wolfson, W. Chiu, A. Sali, Protein structure fitting and refinement guided by cryo-EM density. *Structure* **16**, 295–307 (2008).
68. P. V. Afonine, B. K. Poon, R. J. Read, O. V. Sobolev, T. C. Terwilliger, A. Urzhumtsev, P. D. Adams, Real-space refinement in PHENIX for cryo-EM and crystallography. *Acta Crystallogr. D Struct. Biol.* **74**, 531–544 (2018).

69. C. J. Williams, J. J. Headd, N. W. Moriarty, M. G. Prisant, L. L. Videau, L. N. Deis, V. Verma, D. A. Keedy, B. J. Hintze, V. B. Chen, S. Jain, S. M. Lewis, W. B. Arendall, J. Snoeyink, P. D. Adams, S. C. Lovell, J. S. Richardson, D. C. Richardson, MolProbity: More and better reference data for improved all-atom structure validation. *Protein Sci.* **27**, 293–315 (2018).
70. T. Burnley, C. M. Palmer, M. Winn, Recent developments in the CCP-EM software suite. *Acta Cryst.* **D73**, 469–477 (2017).
71. E. F. Pettersen, T. D. Goddard, C. C. Huang, G. S. Couch, D. M. Greenblatt, E. C. Meng, T. E. Ferrin, UCSF Chimera—A visualization system for exploratory research and analysis. *J. Comput. Chem.* **25**, 1605–1612 (2004).
72. E. F. Pettersen, T. D. Goddard, C. C. Huang, E. C. Meng, G. S. Couch, T. I. Croll, J. H. Morris, T. E. Ferrin, UCSF ChimeraX: Structure visualization for researchers, educators, and developers. *Protein Sci.* **30**, 70–82 (2021).
73. J. R. Kremer, D. N. Mastronarde, J. R. McIntosh, Computer visualization of three-dimensional image data using IMOD. *J. Struct. Biol.* **116**, 71–76 (1996).

Acknowledgments: We thank A. Ciccone and S. Verschoor for perforin preparation, D. Houldershaw for IT support and script writing, and B. Hoogenboom and A. Hodel for comments on the manuscript. **Funding:** This work was funded by ERC grant 294408 and Wellcome Trust grant 106249/Z/14/Z to H.R.S. and Wellcome Trust (209250/Z/17/Z and 208398/Z/17/Z) to M.T. Most of the cryo-EM data for this investigation were collected at the ISMB EM facility at Birkbeck College, University of London with financial support from Wellcome Trust (202679/Z/16/Z and 206166/Z/17/Z). We thank Diamond Light Source for access to the cryo-EM facilities at the UK National electron bio-imaging centre (eBIC, proposal EM14704) funded by the Wellcome Trust, the Medical Research Council UK, and the Biotechnology and Biological Sciences Research Council. **Author contributions:** M.E.I., N.L., J.A.T., I.V., and H.R.S. designed the experiments. M.E.I., N.L., and I.V. collected and analyzed the data. M.E.I., S.M., and M.T. built and refined the atomic model. M.E.I. and H.R.S. wrote the manuscript with input from other authors. **Competing interests:** The authors declare that they have no competing interests. **Data and materials availability:** The final cryo-EM map and corresponding atomic model have been deposited in public repositories with accession codes EMD-13269 and PDB 7PAG, respectively.

Submitted 8 July 2021
Accepted 17 December 2021
Published 11 February 2022
10.1126/sciadv.abk3147